

by an AFM tip, the nanotube region proximal to the tip exhibits significant changes in atomic bonding configuration. For relatively small bending angles ($\theta \leq \sim 7^\circ$), the nanotube retains sp^2 bonding throughout its structure. The nanotube responds elastically but exhibits a larger bond distortion (up to 5.5%) for the atoms in the region underneath the tip than the global strain ($\leq 0.7\%$). This distortion accounts for the initial conductance decrease at small bending angles where the overall simulated structure remains sp^2 . As tip-pushing proceeds, the tube structure progressively evolves and larger structural changes occur underneath the tip. The average number of bonds per atom in the tube section proximal to the tip has increased from 3 to ~ 3.3 for deflection angle $\theta = 11^\circ$ ($\sigma = 1.8\%$) and to 3.6 for $\theta = 15^\circ$ ($\sigma = 3.4\%$). This indicates that the local bonding configuration has changed from sp^2 to nearly sp^3 . Away from the tip region, the nanotube remains essentially in a sp^2 -bonding configuration with bond deformation characterized by the global strain parameter σ . Further local analysis¹⁷ of the bent nanotube in the tip vicinity reveals the onset of an increase in σ -electrons contributing to the local density of states at the Fermi level in the highly deformed local region. This is, however, accompanied by a significant decrease in the π -electron density. As the π -electrons are delocalized and therefore mainly responsible for electrical conduction, a drastic reduction in the π -electron density is responsible for the substantial decrease in conductance. Simulations also find that the local and global deformations of the nanotube are highly reversible (for $\theta < 15^\circ$, $\sigma < 3.4\%$) upon moving the tip away, leading to the recovery of the nanotube structure and electrical conductance. These results are in excellent agreement with our experimental observations.

The deviation of force versus deflection $F(\delta)$ curve from the δ^3 -relation for $\sigma > \sim 0.3\%$ ($\theta > \sim 5^\circ$, Fig. 2) should be owing to large local-strain developed in the sp^3 region proximal to the tip, as the elastic string model assuming a homogeneous global strain becomes invalid. This is consistent with the electromechanical behaviour that beyond the elastic response regime ($\theta > \sim 5^\circ$, Fig. 4a, inset), tip-forced sp^3 bonding within the nanotube occurs, causing a significant decrease in the nanotube conductance.

Previous theoretical investigations indicate that the electrical properties of metallic SWNTs should be insensitive to small bending deformations^{2,4,18}. The calculated conductance of a (5,5) SWNT changes very little for bending angles up to $\theta = 24^\circ$, when bending at the centre of the SWNT is modelled by holding the ends of the tube at fixed positions to define the bending angle without the involvement of a tip³. This results in a situation where the atomic bonding characteristics of the bent nanotube still remain sp^2 . The absence of sp^3 bonding in the simulated structure should account for the small electrical conductance change³. A similar bending technique¹⁸ found that the electrical conductance of a metallic (6,6) SWNT did not change significantly for bending angles up to $\theta \sim 22.5^\circ$. At larger bending angles (for example $\theta = 45^\circ$) the conductance of the SWNT was lowered by at most tenfold. The conductance decrease is explained by σ - π hybridization effects owing to the increased curvature under high bending angles¹⁸.

Here we used an AFM tip both in experiments and in simulations, a key to performing the experimental measurements and obtaining a fundamental understanding. Our work elucidates the electromechanical properties of the nanotube when mechanical action of a local probe causes a large local deformation. This differs from previous considerations of deformed nanotubes in which the nanotube structure is more or less uniformly bent or strained (at least in the bending-angle range investigated here). The experimental investigation of uniform global strain or bending effects requires different nanotube manipulation mechanisms, such as electrostatic forces¹⁹. We believe that the physics presented here should hold for SWNTs containing large local deformations caused by other forces. For instance, if a highly kinked SWNT stabilized by van der Waals forces on a substrate develops sp^3 bonding character-

istics at the kink, the electrical conductance should be significantly reduced compared to a straight tube. □

Received 8 December 1999; accepted 20 April 2000.

- Crespi, V., Cohen, M. & Rubio, A. *In situ* band gap engineering of carbon nanotubes. *Phys. Rev. Lett.* **79**, 2093–2096 (1997).
- Kane, C. L. & Mele, E. J. Size, shape, and low energy electronic structure of carbon nanotubes. *Phys. Rev. Lett.* **78**, 1932–1935 (1997).
- Nardelli, M. & Bernholc, J. Mechanical deformations and coherent transport in carbon nanotubes. *Phys. Rev. B*, **60**, R16338–R16341 (1998).
- Rocheffort, A., Salahub, D. & Avouris, P. The effect of structural distortions on the electronic structure of carbon nanotubes. *Chem. Phys. Lett.* **297**, 45–50 (1998).
- Bezryadin, A., Verschuere, A., Tans, S. & Dekker, C. Multiprobe transport experiments on individual single-wall carbon nanotubes. *Phys. Rev. Lett.* **80**, 4036–4039 (1998).
- Paulson, S. *et al.* *In situ* resistance measurements of strained carbon nanotubes. *Appl. Phys. Lett.* **75**, 2936–2938 (1999).
- Kong, J., Soh, H., Cassell, A., Quate, C. F. & Dai, H. Synthesis of individual single-walled carbon nanotubes on patterned silicon wafers. *Nature* **395**, 878–881 (1998).
- Soh, H. *et al.* Integrated nanotube circuits: controlled growth and ohmic contacting of single-walled carbon nanotubes. *Appl. Phys. Lett.* **75**, 627–629 (1999).
- Kong, J. *et al.* Synthesis, integration and electrical properties of individual single-walled carbon nanotubes. *Appl. Phys. A* **69**, 305–308 (1999).
- Salvetat, J. P. *et al.* Elastic and shear moduli of single-walled carbon nanotube ropes. *Phys. Rev. Lett.* **82**, 944–947 (1999).
- Timoshenko, S. *Strength of Materials. Part I, Elementary Theory and Problems* (Van Nostrand, New York, 1930).
- Walters, D. *et al.* Elastic strain of freely suspended single-walled carbon nanotube ropes. *Appl. Phys. Lett.* **74**, 3803–3805 (1999).
- Hertel, T., Martel, R. & Avouris, P. Manipulation of individual carbon nanotubes and their interaction with surfaces. *J. Phys. Chem.* **102**, 910–915 (1998).
- Jayanthi, C. S. *et al.* Order-N method for a nonorthogonal tight-binding Hamiltonian. *Phys. Rev. B* **57**, 3799–3802 (1998).
- Datta, S. *Electronic Transport in Mesoscopic Systems*. (University Press, Cambridge, 1995).
- Wu, S. Y. & Jayanthi, C. S. Local analysis via the real space greens function method. *J. Modern Phys.* **B 9**, 1869–1897 (1995).
- Alfonso, D., Wu, S. Y., Jayanthi, C. S. & Kaxiras, E. Linking chemical reactivity, magic numbers, and local electronic properties of clusters. *Phys. Rev. B* **59**, 7745–7750 (1999).
- Rocheffort, A., Lesage, F., Salhub, D. & Avouris, P. Conductance of distorted carbon nanotubes. *Phys. Rev. B*, **60**, 13824–13830 (1999).
- Kim, P. & Lieber, C. Nanotube nanotweezers. *Science* **286**, 2148–2150 (1999).

Acknowledgements

We thank C. Quate for discussions and use of equipment. This work was supported by the Defense Advanced Research Projects Agency/Office of Naval Research, National Science Foundation, Semiconductor Research Corporation/Motorola, a David and Lucile Packard Fellowship, a Terman Fellowship, the Laboratory for Advance Materials at Stanford, National Nanofabrication Users Network at Stanford, the Camille Henry-Dreyfus Foundation, the American Chemical Society and the University of Kentucky Center for Computer Sciences.

Correspondence and requests for materials should be addressed to H.D. (email: hdai@chem.stanford.edu).

Controlling droplet deposition with polymer additives

Vance Bergeron[†], Daniel Bonn[‡], Jean Yves Martin[†] & Louis Vovelle[†]

[†] Rhodia Recherches, Centre de Recherches Lyon, 85 Av. Des Freres Perret-BP62, 69192 Saint-Fons Cedex, France

[‡] Ecole Normale Supérieure, Laboratoire de Physique Statistique, 24 rue Lhomond, 75231 Paris Cedex 05, France

Controlling the impact of drops onto solid surfaces is important for a wide variety of coating and deposition processes—for example, the treatment of plants with herbicides and pesticides requires precise targeting in order to meet stringent toxicological regulations. However, the outer wax-like layer of the leaves is a non-wetting substrate that causes sprayed droplets to rebound; often less than 50% of the initial spray is retained by the plant¹. Although the impact and subsequent retraction of non-wetting aqueous drops on a hydrophobic surface have been the subjects of

extensive experimental and theoretical work²⁻⁷, non-newtonian rheological effects have not been considered in any detail. Here we report that, by adding very small amounts of a flexible polymer to the aqueous phase, we can inhibit droplet rebound on a hydrophobic surface and markedly improve deposition without significantly altering the shear viscosity of the solutions. Our results can be understood by taking into account the non-newtonian elongational viscosity, which provides a large resistance to drop retraction after impact, thereby suppressing droplet rebound.

High-velocity drops colliding with a solid non-wetting surface impact, expand and subsequently retract (Fig. 1). Previous work has focused on the very rapid impact and expansion stages in an effort to determine the maximum diameter, D_{max} , that a drop is capable of attaining on impact for optimizing deposition^{2,5,6}. These studies have shown that for newtonian fluids the impact and expansion stages are governed by the Reynolds number, $Re = DV_1\rho/\eta_s$, which is a ratio of inertial to viscous forces, and the Weber number, $We = \rho V_1^2 D/\sigma$, which is a balance between inertial and capillary forces, where D is the drop diameter, V_1 is the drop velocity at impact, ρ is the drop density, η_s is the solution shear viscosity and σ is the surface tension of the solution. In general, the contact angle of the liquid on the substrate and surface roughness must also be considered when describing the impact events of drops.

Here we use only smooth, non-wetting hydrophobic surfaces, all with a receding contact angle greater than 120° . Furthermore, we use large drops (~ 2 mm) striking at high velocities, which leads to inertially dominated impact and expansion stages. This not only corresponds to most practical situations but also allows us to control the first two stages of the impact, that is, that all drops in this study expand to the same maximum diameter⁵. We are therefore able to focus on the final drop-retraction stage of the process which determines whether or not a deposited drop rebounds off the surface.

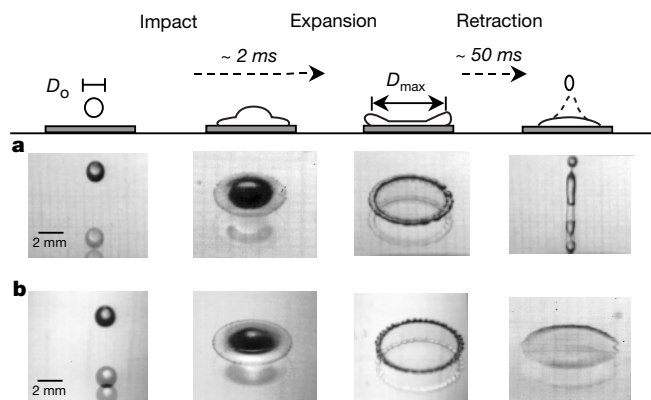


Figure 1 Typical photographic sequence (left to right) of two aqueous drops striking a hydrophobic surface. In each case focus should be placed on the uppermost image; the lower ghost images are reflections from the top and/or bottom surface of the solid glass substrate. Impact and expansion from the initial undeformed drop diameter, D_0 , to the maximum spread diameter, D_{max} , occurs in the first 2 ms. Subsequently, the drops retract and can either detach from the surface (a, pure water) or remain bound to the surface after impact (b, dilute polyethyleneoxide solution, molecular weight 4×10^6 g mol⁻¹, at 0.1 g l⁻¹). We visualize these events with a 1,000 frame s⁻¹ video recording system (NAC HSV-1000). Drops are produced using a syringe pump, extruding the solution through a stainless-steel needle, the diameter of which determines the drop size. Impact velocities are imposed by the height of the needle above the horizontally placed hydrophobic surface. These surfaces are prepared by spin-coating 1×1 cm, acid-washed glass plates with a 0.4 g ml⁻¹ solution of a stearic acid complexing agent, Rhodoline EP 9271 (Rhodia Specialty Chemicals). This produces a smooth coating with an air-solution receding contact angle greater than 120° , both before and after impact, for all of our solutions. This last point verifies that specific adsorption of material (that is, polymer) upon drop impact does not lead to surface modification during the impact event, which is known to influence the wettability of the surface in certain circumstances^{15,16}.

We find that droplet rebound from non-wetting surfaces can be markedly suppressed by small amounts of a polymer additive. High-speed photography reveals similar impact and expansion stages for both pure water and dilute polymer solutions, yet the retraction phase is very different. For pure water (Fig. 1a) the drop retracts violently, leading to ejection of part of the droplet from the surface, that is, drop rebound occurs; however, for dilute aqueous solutions of a flexible polymer (for example, polyethyleneoxide; Fig. 1b) the drop retracts much more slowly and remains deposited on the surface.

The photographic sequences in Fig. 1 are transformed into 'drop-evolution' plots by recording the drop diameter on the surface over time (Fig. 2). These plots permit us to define a retraction velocity, V_{ret} , from which we can quantitatively gauge the drop-retraction phase. Notably, droplet rebound occurs if the retraction speed is beyond a certain critical value, $V_{ret} > 300$ mm s⁻¹, not attained for the polymeric solutions.

Compared with the inertially dominated impact and expansion stages, which occur over the first 2 ms, the flow during the retraction stage is nearly an order of magnitude slower. This fact is quantitatively revealed by comparing the Reynolds and Weber numbers for pure water droplets during the expansion and retraction stage: $Re_{expansion}/Re_{retraction} \approx 6,000/1,200$, $We_{expansion}/We_{retraction} \approx 250/10$, the difference resulting from a fivefold decrease in the retraction velocity relative to the drop-impact velocity. It follows that drop inertia dominates during the expansion stage, although, to a good approximation, it can be neglected with respect to viscosity effects during the retraction stage: for newtonian liquids, the retraction speed is governed by the capillary number, $Ca = V_{ret}\eta_s/\sigma$ (ref. 8), where V_{ret} is the retraction velocity. Ca represents the competition between the viscous forces that tend to slow down the retraction, and the capillary forces (that is, surface tension) that act to contract the drop and accelerate retraction. Thus, systematically comparing the Ca values of a series of aqueous newtonian solutions with those of their non-newtonian counterparts (that is, solutions with the same shear viscosity and surface tension) allows us to test the influence that non-newtonian rheological properties have on droplet rebound.

The dependence of Ca on drop-retraction speed for the case of newtonian fluids is obtained by changing the shear viscosity using water-glycerol mixtures (Fig. 3). Experimental aspects of this case have been previously reported⁹. For dilute polymer solutions the

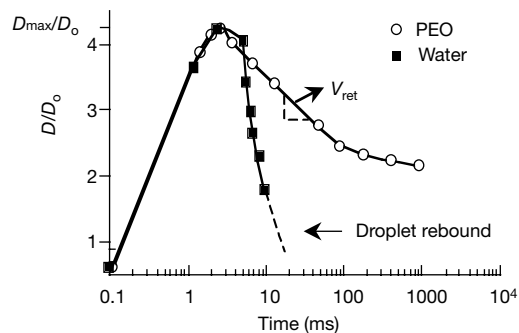


Figure 2 Drop diameter versus time. Filled squares represent a pure water droplet, open circles represent a dilute aqueous solution of polyethyleneoxide (PEO; 0.1 g l⁻¹ of molecular weight 4×10^6 g mol⁻¹); lines are provided as a guide to the eye. Analysis of the full data from all of our high-speed footage shows that to within experimental error the spreading velocities are identical during the impact and expansion stages. Drop-retraction velocity, V_{ret} , is defined as the slope of the spread radius versus time after maximum drop expansion. The characteristic V_{ret} for each drop is determined by making a linear approximation of the initial linear portion of the decaying region of the data. Dashed lines extending from the pure water data indicate that a portion of the droplet has pinched off the surface.

behaviour is different. Here the level of polymer is systematically changed, but the shear viscosity and surface tension for these dilute solutions (between 0.01 and 0.5 g l^{-1} polyethyleneoxide) remain very similar to those of pure water. The subsequent Ca versus V_{ret} correlation between the newtonian fluids and the dilute polymer solutions diverges. This clearly shows that non-newtonian effects need to be considered. Specifically, owing to the highly elongational nature of the flow within the retracting droplets, the predominant effect is due to the high elongational viscosity, η_e , provided by the flexible polymers in solution (see below).

In determining the resistance to stretching motion in a fluid, the so-called 'elongational' or extensional viscosity has been and remains a significant problem in non-newtonian fluid mechanics in general, and for dilute solutions in particular¹⁰. We obtain the elongational viscosity of our solutions in two different ways: first, by using an opposing-jet rheometer¹¹; and second, by using a technique that exploits the use of hydrodynamic constitutive equations. Fitting an appropriate constitutive equation to direct measurements of the shear viscosity and normal stress difference provides the information needed to evaluate the solution's elongational viscosity. Our measurements are obtained in simple shear flow using a custom-made cone-plate geometry which allows access to the high shear rates that are necessary to measure the elastic response of the dilute polymer solutions. The data are then fitted to the so-called 'FENE-P' (finitely extendible nonlinear elastic) constitutive equation^{12,13}; a relatively simple model in which the polymer molecules are represented as dumb-bells that can be stretched by a finite amount in the flow field. Values of the elongational viscosity obtained in this way are compared with the measurements using a Rheometrics RFX opposing nozzle rheometer referenced to pure water (Fig. 4). Although there has been much discussion concerning the validity of measurements obtained with such opposing-nozzle devices^{10,11}, the agreement with the FENE-P model calculations is satisfactory (see Fig. 4). This is probably because our polymer solutions are very dilute and have shear viscosities close to that of water.

The characteristic elongation rate of the retracting drops can be obtained from the rim velocity ($\sim 30 \text{ cm s}^{-1}$) divided by the thickness of the stretched droplet ($\sim 0.1 \text{ mm}$). This leads to typical elongation rates of $\epsilon \approx 3,000 \text{ s}^{-1}$. With reference to the measurements of the elongational viscosity versus elongation rate (Fig. 4), it is evident that the high- ϵ plateau for η_e should be taken as the characteristic elongational viscosity during our drop-impact experiments.

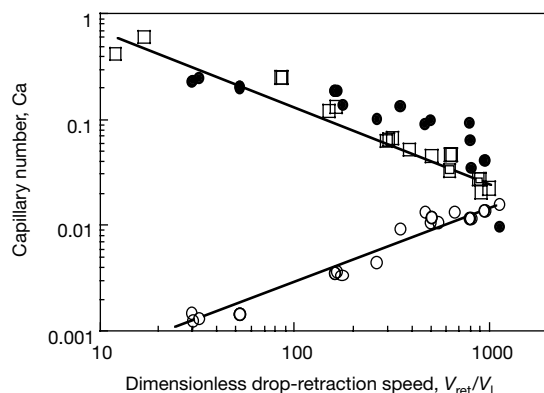


Figure 3 Capillary number versus non-dimensional drop-retraction speed, (V_{ret}/V_l), of the droplets; squares represent water-glycerol mixtures and circles represent polymer solutions of different concentrations. Open symbols denote that the capillary number has been calculated using the shear viscosity: a strong disagreement with the newtonian data is found in this case, as highlighted by the solid lines. In contrast, the agreement is very good when the capillary number is calculated using the elongational viscosity (filled circles).

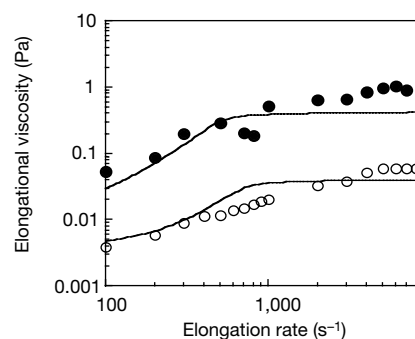


Figure 4 Elongational viscosity versus elongation rate. Measurements made with a Rheometrics RFX opposing nozzle for two dilute PEO polymer solutions are shown: 0.25 g l^{-1} , molecular weight 4×10^6 (filled circles); 1.0 g l^{-1} , molecular weight 2×10^6 (open circles). Lines represent the corresponding FENE-P model calculations. A Rheologica Stress-Tech rheometer equipped with a cone-plate geometry was used to obtain the data needed for our FENE model calculations. The cone is 55 mm in diameter and has an angle of 0.5° , which allows the measurement of extremely small normal forces at very high shear rates. We have experimentally determined by viscosity measurements that the overlap concentration, c^* , is about 0.5 g l^{-1} for our polymer solutions. This indicates a concentration of 0.5 g l^{-1} as the experimentally determined value for the dilute regime and that nearly all of the experiments shown fall within the so-called 'dilute regime' for the conditions of our study.

Evidence that the elongational viscosity is the predominant factor influencing the difference in drop-retraction behaviour between the newtonian and non-newtonian solutions can be demonstrated by reformulating the capillary number using the elongational, rather than the shear viscosity. Thus, we define the capillary number for our retracting drops as $Ca_e = V_{\text{ret}}\eta_e/3\sigma$, noting that the elongational viscosity for newtonian liquids is given by $\eta_e = 3\eta_s$. If the capillary number is recalculated in this way, the results for the dilute polymer solutions coincide with those of the newtonian solutions (Fig. 3). Therefore, we see that here it is the elongational viscosity that dominates during drop retraction, consequently inhibiting droplet rebound.

Finally, we note that our observations are general and that we have observed the same phenomena for different hydrophobic surfaces: polished Teflon and paper hydrophobized by treatment with polydimethylsilicone (for example, 'Silkraf 9564' from Ahlstrom). In addition, other dilute solutions of high molecular weight flexible polymers, such as locus-bean and guar gum, manifest high elongational viscosities and significantly reduce droplet rebound¹⁴. Significant improvements in drop deposition on rough surfaces has also been witnessed, however, rigorous quantification of these effects remains the subject of future work.

In conclusion, we have shown that drop rebound, a major problem in a number of industrial applications, can be inhibited very effectively by the addition of small amounts of a flexible polymer. We have also shown that the critical property provided by these polymers is a high elongational viscosity. This non-newtonian property dampens the drops' retraction after impact, which in turn prevents droplet rebound. We propose and validate a simple way of evaluating the elongational viscosity of dilute solutions of flexible polymers. The solutions can be very dilute, so that the shear viscosity is essentially the same as that of the solvent. This last point has important practical implications, as drop impact will nearly always be preceded by other processes (for example, pumping) for which a low shear viscosity is needed. □

Received 30 September 1999; accepted 27 April 2000.

- Wirth, W., Storp, S. & Jacobsen, W. Mechanisms controlling leaf retention of agricultural spray solutions. *Pest. Sci.* **33**, 411–422 (1991).
- Chandra, S. & Avedisian, C. T. On the collision of a droplet with a solid surface. *Proc. R. Soc. Lond. A* **432**, 13–41 (1991).

3. Rein, M. Phenomena of liquid drop impact on solid and liquid surfaces. *Fluid Dynamics Res.* **12**, 61–93 (1993).
4. Fukai, J. *et al.* Wetting effects on the spreading of a liquid droplet colliding with a flat surface: experiment and modeling. *Phys. Fluids* **7**, 236–247 (1995).
5. Bennett, T. & Poulikakos, D. Splat–quench solidification: estimating the maximum spreading of a droplet impacting a solid surface. *J. Mater. Sci.* **28**, 963–970 (1993).
6. Scheller, B. L. & Bousfield, D. W. Newtonian drop impact with a solid surface. *Am. Inst. Chem. Eng. J.* **41**, 1357–1367 (1995).
7. Mao, T., Kuhn, D. & Tran, H. Spread and rebound of liquid droplets upon impact on flat surfaces. *Am. Inst. Chem. Eng. J.* **43**, 2169–2179, (1997).
8. de Gennes, P. G. Wetting: statics and dynamics. *Rev. Mod. Phys.* **57**, 827–863 (1985).
9. Hayes, R. A. & Ralston, J. Forced liquid movement on low energy surfaces. *J. Colloid Interface Sci.* **159**, 429–438 (1993).
10. Hudson, N., & Jones, T. The A1 projet—an overview. *J. Non-Newtonian Fluid Mech.* **46**, 69–88 (1993).
11. Dontula, P., Pasquali, M., Scriven, L. E. & Macosko, C. W. Can extensional viscosity be measured with opposed-nozzle devices? *Rheol. Acta* **36**, 429–448 (1997).
12. Bird, R. B., Armstrong, R. C. & Hassager, O. in *Dynamics of Polymeric Liquids* Vols 1, 2, pp 495–520 (Wiley, New York, 1987).
13. Tanner, R. I. in *Engineering Rheology* 168–224 (Clarendon, Oxford, 1992).
14. Bergeron, V., Martin, J.-Y. & Vovelle, L. Utilisation de polymères comme agents anti-rebond dan des formulations mises en œuvre en milieux aqueux. French Patent Application 9810471 (1998); International Extension PCT/FR99/02002 (1999).
15. Yerushalmi-Rozen, R., Klein, J. & Fetters, L. J. Suppression of rupture in thin, nonwetting liquid films. *Science* **263**, 793–795 (1994).
16. Yerushalmi-Rozen, R. & Klein, J. Stabilization of non-wetting thin liquid films on a solid substrate by polymeric additives. *Langmuir* **11**, 2806–2814 (1995).

Acknowledgements

D.B. thanks S. Kumar for helpful discussions; and J. Vermant and P. Moldenaers for help with the elongational viscosity measurements. LPS de l’ENS is UMR 8550 of the CNRS, associated with the universities Paris 6 and 7. We also thank the European Commission for their support in the form of TMR project funding.

Correspondence and requests for materials should be addressed to V.B. (e-mail: vance.bergeron@rhone-poulenc.com).

Significant dissipation of tidal energy in the deep ocean inferred from satellite altimeter data

G. D. Egbert* & R. D. Ray†

* College of Oceanic and Atmospheric Sciences, Oregon State University, Corvallis, Oregon 97331, USA

† NASA Goddard Space Flight Center, Code 926, Greenbelt, Maryland 20771, USA

How and where the ocean tides dissipate their energy are long-standing questions¹ that have consequences ranging from the history of the Moon² to the mixing of the oceans³. Historically, the principal sink of tidal energy has been thought to be bottom friction in shallow seas^{4,5}. There has long been suggestive evidence^{6,7}, however, that tidal dissipation also occurs in the open ocean through the scattering by ocean-bottom topography of surface tides into internal waves, but estimates of the magnitude of this possible sink have varied widely^{3,8–11}. Here we use satellite altimeter data from Topex/Poseidon to map empirically the tidal energy dissipation. We show that approximately 10¹² watts—that is, 1 TW, representing 25–30% of the total dissipation—occurs in the deep ocean, generally near areas of rough topography. Of the estimated 2 TW of mixing energy required to maintain the large-scale thermohaline circulation of the ocean¹², one-half could therefore be provided by the tides, with the other half coming from action¹³ on the surface of the ocean.

Vertical mixing rates in the deep ocean implied by ocean microstructure¹⁴ and tracer-release data¹⁵ are typically an order of magnitude too small to balance the rate at which dense bottom

water is created at high latitudes¹². It has thus been suggested that much of the mixing required to maintain the abyssal stratification, and hence the large-scale meridional overturning, occurs at localized ‘hotspots’ near areas of rough topography^{4,16,17}. Numerical modelling studies further suggest that the ocean circulation is sensitive to the spatial distribution of vertical mixing¹⁸. Thus, clarifying the physical mechanisms responsible for this mixing is important, both for numerical ocean modelling and for general understanding of how the ocean works. One significant energy source for mixing may be barotropic tidal currents. The likelihood of this depends *inter alia* on whether enough power is being extracted from the barotropic tides in the likely ‘hotspot’ regions. Topex/Poseidon (T/P) satellite altimeter data have now made possible accurate mapping of open-ocean tidal elevations¹⁹, and provide a new opportunity to quantify empirically the spatial localization of tidal dissipation.

Here we concentrate on the principal lunar semi-diurnal tide M₂, which accounts for approximately two-thirds of the total planetary dissipation²⁰, and is the most accurately known tide. This accuracy is needed, because mapping dissipation involves second-order gradients of measured fields and small differences of large numbers.

The barotropic ocean tide satisfies the tidal equations of Laplace, modified to include effects of an elastic Earth and a self-gravitating ocean²¹. These equations embody conservation of momentum and mass for the ocean fluid:

$$\frac{\partial \mathbf{U}}{\partial t} + \mathbf{f} \times \mathbf{U} = -gH\nabla(\zeta_{EQ} - \zeta_{SAL}) - F \tag{1}$$

$$\frac{\partial \zeta}{\partial t} = -\nabla \cdot \mathbf{U} \tag{2}$$

Here ζ is the tidal elevation; \mathbf{U} is the volume transport vector, equal to velocity times water depth H ; \mathbf{f} is the Coriolis parameter (oriented to the local vertical), and F is a generic frictional or dissipative stress. The forcing is specified through an equilibrium tide ζ_{EQ} , which must allow for the Earth’s body tide²¹, and an equilibrium-like ‘tide’ ζ_{SAL} which is induced by the tide’s self-attraction and loading²².

Equations (1) and (2) may be combined and averaged over time to obtain an expression for the local balance between work rate, W , energy flux, \mathbf{P} , and dissipation rate, D :

$$W - \nabla \cdot \mathbf{P} = D \tag{3}$$

A number of different explicit forms for this balance appear in the literature^{21,23}, reflecting various groupings of terms, and different definitions for work and flux (as well as omission of supposed secondary terms like self-attraction). Here we adopt simple expressions for these terms based directly on equations (1) and (2):

$$\mathbf{P} = \rho g \langle \mathbf{U} \zeta \rangle \quad W = \rho g \langle \mathbf{U} \cdot \nabla (\zeta_{EQ} + \zeta_{SAL}) \rangle \tag{4}$$

where the brackets $\langle \rangle$ denote time averages, ρ is mean seawater density and g is gravitational acceleration. Note that W represents the mean rate of working on the ocean of all tidal gravitational forces (including self-attraction forces) and of the moving ocean bottom.

Topex/Poseidon altimeter data provide a direct constraint on tidal elevations ζ , and a number of nearly global maps are now

Table 1 Partition of M₂ energy dissipation (in terawatts) between shallow seas and the deep ocean

	TPXO.4a	GOT99hf	TPXO.4b	TPXO.4c	GOT99nf	Prior	Error
Shallow seas	1.60	1.71	1.61	1.62	1.87	1.96	0.06
Deep ocean	0.83	0.74	0.82	0.81	0.57	0.06	0.06
Total	2.44	2.45	2.43	2.43	2.44	2.02	0.01

Results (in TW) are presented for the five empirical estimates discussed in the text, and for the purely hydrodynamic solution used as the prior model for the assimilation. Error bars²⁸ are for the assimilation solution TPXO.4a. Here shallow seas are defined to include all ocean areas landward of the thin line in Fig. 1b.